










Ground Calibration of Solar X-ray Monitor On-board Chandrayaan-2 Orbiter

N. P. S. Mithun  · Santosh V. Vadawale  · M. Shanmugam · Arpit R. Patel  · Neeraj Kumar Tiwari · Hiteshkumar L. Adalja · Shiv Kumar Goyal  · Tinkal Ladiya · Nishant Singh · Sushil Kumar · Manoj K. Tiwari  · M. H. Modi · Biswajit Mondal · Aveek Sarkar  · Bhuwan Joshi  · P. Janardhan  · Anil Bhardwaj 

Received: date / Accepted: date

Abstract Chandrayaan-2, the second Indian mission to the Moon, carries a spectrometer called the *Solar X-ray Monitor* (XSM) to perform soft X-ray spectral measurements of the Sun while a companion payload measures the fluorescence emission from the Moon. Together these two payloads will provide quantitative estimates of elemental abundances on the lunar surface. XSM is also expected to provide significant contributions to the solar X-ray studies with its highest time cadence and energy resolution spectral measurements. For this purpose, the XSM employs a Silicon Drift Detector and carries out energy measurements of incident photons in the 1 – 15 keV range with a resolution of <180 eV at 5.9 keV, over a wide range of solar X-ray intensities. Extensive ground calibration experiments have been carried out with the XSM using laboratory X-ray sources as well as X-ray beam-line facilities to determine the instrument response matrix parameters required for quantitative spectral analysis. This includes measurements of gain, spectral redistribution function, and effective area, under various observing conditions. The capability of the XSM to maintain its spectral performance at high incident flux as well as the dead-time and pile-up characteristics have also been investigated. The results

N. P. S. Mithun
E-mail: mithun@prl.res.in

N. P. S. Mithun · Santosh V. Vadawale · M. Shanmugam · Arpit R. Patel · Neeraj Kumar Tiwari · Hitesh Kumar L. Adalja · Shiv Kumar Goyal · Tinkal Ladiya · Nishant Singh · Sushil Kumar · Biswajit Mondal · Aveek Sarkar · Bhuwan Joshi · P. Janardhan · Anil Bhardwaj
Physical Research Laboratory, Ahmedabad, Gujarat, India

Manoj K. Tiwari · M. H. Modi
Raja Ramanna Centre for Advanced Technology, Indore, Madhya Pradesh, India

of these ground calibration experiments of the XSM payload are presented in this article.

Keywords Instrumentation: Spectroscopy, Calibration · Space vehicles: Instruments · Sun: X-rays

1 Introduction

The Chandrayaan-2 mission [1] includes a remote X-ray fluorescence spectroscopy experiment to obtain quantitative estimates of the elemental abundances on the lunar surface. This experiment has been realized with two instruments onboard the Chandrayaan-2 orbiter viz. (i) the *Chandrayaan-2 Large Area Soft X-ray Spectrometer* (CLASS) [2], which measures the X-ray fluorescence from the elements on the lunar surface; and (ii) the *Solar X-ray Monitor* (XSM) [3], which measures the spectrum of solar X-rays responsible for excitation of the elements on the lunar surface. From the strength of elemental lines obtained from the CLASS spectrum together with the incident solar spectrum inferred from the XSM, the quantitative estimates of abundances of constituent elements on the lunar surface can be derived. Apart from this, with unique characteristics such as the highest spectral resolution for a solar broadband soft X-ray spectrometer and the full resolution spectral measurement at every second, the XSM is also expected to provide significant contributions to enhance our understanding of the corona, the outer atmosphere of the Sun.

The XSM is designed to carry out spectroscopy of the Sun in the 1–15 keV energy range, and the basic measurement from the instrument is the number of events registered in each instrument channel in every one-second time interval. However, the elemental analysis as well as any independent investigations of the Sun would require estimation of the incident solar spectrum, in physical units, from this observed raw spectrum, which requires knowledge of various factors contributing to the instrument response. Uncertainties in the estimates of physical parameters of the source from these observations would critically depend on how well the instrument response has been calibrated. In the case of a space-based experiment like XSM, the calibration activities involve both the ground calibration where specific experiments are carried out to determine all the instrument parameters and the in-flight calibration where these parameters are validated and further refined.

This article presents an overview of the Chandrayaan-2 XSM instrument and the results of its ground calibration. Section 2 describes the instrument and the calibration requirements are discussed in section 3. Sections 4 - 8 describe the calibration experiments and their results followed by a summary in section 9.

Table 1 Specifications of XSM

Parameter	Specification
Energy Range	1 – 15 keV (up to $\sim 80,000$ counts s^{-1}) 2 – 15 keV (above $\sim 80,000$ counts s^{-1})
Energy Resolution	< 180 eV @ 5.9 keV
Time cadence	1 second
Aperture area	0.367 mm ²
Field of view	± 40 degree
Filter wheel mechanism properties	
Positions	3 (Open, Be-filter, Cal)
Filter wheel movement modes	Automated and Manual
Be-filter thickness	250 μ m
Automated Be-filter movement threshold	$80,000$ counts s^{-1}
Calibration source	Fe-55 with Ti foil
Detector properties	
Type	Silicon Drift Detector (SDD)
Area	30 mm ²
Thickness	450 μ m
Entrance Window	8 μ m thick Be
Operating temperature	-35° C
Electronics parameters	
Pulse shaping time	1 μ s
Dead time	5 μ s
Number of channels in the spectrum	1024
Mass	1.35 kg
Power	6 W

2 XSM on-board Chandrayaan-2

The XSM carries out spectral measurements of the Sun in soft X-rays with an energy resolution better than 180 eV at 5.9 keV. Major specifications of the XSM instrument are given in table 1, and a detailed description of the instrument design can be seen in Shanmugam *et al.*, 2020 [3]. Figure 1 shows a photograph of the XSM instrument which is configured as two packages: (i) a sensor package that houses the detector, front-end electronics, and a filter wheel mechanism; (ii) a processing electronics package that houses the FPGA based data acquisition system, power electronics, and spacecraft interfaces. The instrument is fix-mounted on the Chandrayaan-2 orbiter such that the spacecraft structures do not obstruct the instrument field of view (FOV). Figure 2 shows the mounting of XSM packages on the spacecraft and definitions of the spacecraft and instrument reference frames.

At the heart of the instrument is a Silicon Drift Detector (SDD). Its unique configuration of electrodes provides very low detector capacitance and, thereby, higher spectral resolution than other silicon-based detectors that work in a similar energy range. The SDD also has the ability to handle relatively higher incident flux. The detector, procured from KETEK GmbH, Germany, is available in the form of an encapsulated module containing a thermo-electric cooler (TEC), a FET, a temperature diode, and an 8 μ m thick Beryllium entrance window. The detector has an active area of ~ 30 mm² and a thickness of 450 μ m.

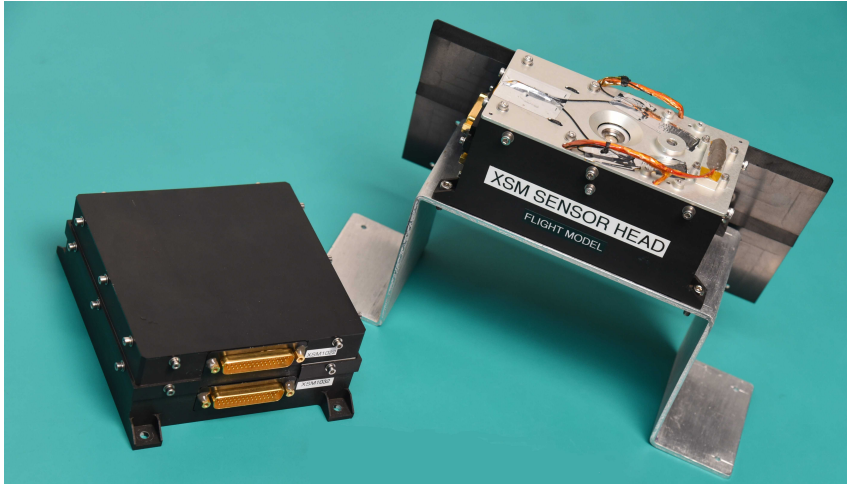


Fig. 1 A photograph of the Chandrayaan-2 XSM instrument packages: (i) sensor package that houses the detector, front-end electronics, and filter wheel mechanism (right) ; (ii) processing electronics package that houses the FPGA based data acquisition system, power electronics, and spacecraft interfaces (left).

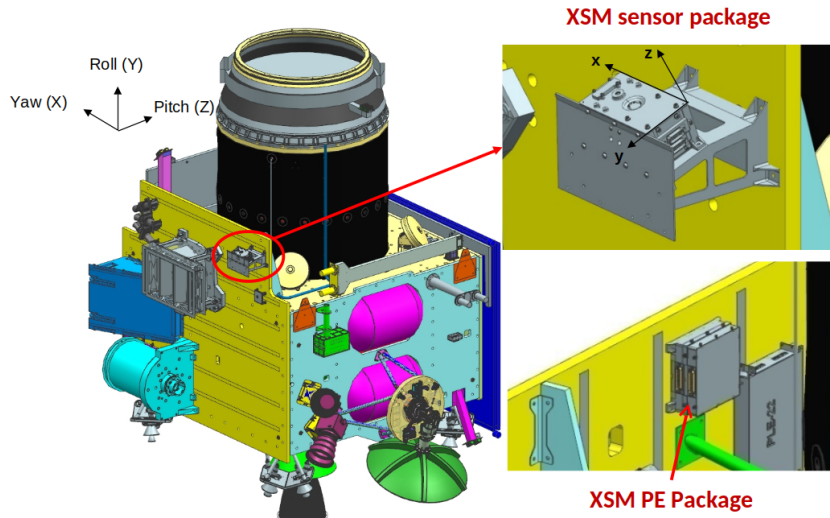


Fig. 2 Schematic representation of Chandrayaan-2 orbiter showing the mounting location of the XSM sensor and processing electronics (PE) packages. The spacecraft reference frame axes, Yaw(X), Roll(Y), and Pitch(Z), are marked in the figure. The sensor package is mounted on the -pitch panel of the spacecraft with a canted bracket (20° from roll axis towards -pitch direction) to avoid any spacecraft structures obstructing its field of view. The PE package is mounted on the inner side of the -pitch panel. Axis definitions for the XSM instrument reference frame are marked on the sensor package. The XSM reference frame is obtained by a rotation of -110° about the X-axis of the spacecraft frame.

X-ray photons incident on the SDD generate a charge cloud proportional to the deposited photon energy, which is collected at the anode of the detector. The front-end electronics that include a charge sensitive preamplifier and shaping amplifiers convert this charge to a voltage signal in the form of a semi-Gaussian pulse. The peak of this pulse is then detected by a peak detector and digitized by a 12-bit analog to digital converter (ADC). Histograms of the 10-bit ADC channels (ignoring the two least significant bits), where each channel is ~ 16.5 eV wide, are generated at an interval of one second and is recorded on-board. Apart from the complete spectrum with one-second cadence, the XSM also records light curves in three pre-defined, but adjustable (by ground command), energy intervals with a 100 ms time resolution. XSM processing electronics packetizes the spectral data every second along with the health parameters of the instrument, such as the detector temperature, current drawn by the TEC, and various voltage levels. These packets are sent to the spacecraft data handling system that records it after tagging it with the onboard clock time. Absolute time is assigned to each data packet during ground processing by the correlation between onboard clock time and Coordinated Universal Time (UTC) from the available real-time telemetry.

The spectral performance of the detector, defined by the energy resolution, depends on its temperature. In order to achieve the targeted resolution of better than 180 eV, the SDD temperature needs to be maintained at $\sim -35^\circ\text{C}$. Since the ambient temperature during the lunar orbit is expected to vary over a wide range between -30°C to $+20^\circ\text{C}$, the XSM employs a closed-loop temperature control using the TEC that is part of the detector module, to maintain the detector at -35°C . The hot end of the TEC is interfaced with a thermal radiator to radiate away the heat. There is also a provision to vary the set point of the detector temperature by ground command, in case such a requirement arises.

It is well known that the solar X-ray intensities vary over several orders of magnitude between quiet and active phases of a solar cycle [4]. In the classification of solar flares based on the flux measured by the GOES 1–8 Å channel, the highest intensity X-class flares have five orders of magnitude higher flux than the lowest intensity A-class flares. A single X-ray spectroscopic detector cannot be sensitive enough to detect flares below A-class and, at the same time, does not saturate during large flares. Hence, the XSM includes a filter wheel mechanism mounted on the top cover of the sensor package that brings a 250 μm Beryllium filter in front of the detector during high-intensity flares. This additional Be filter increases the low energy cutoff and thereby reduces the incident rate. An onboard algorithm moves the filter wheel to the Be-filter position when the count rate is higher than the specified threshold for five consecutive intervals of 100 ms. A similar automated logic decides the movement of the filter wheel mechanism back to its open position. The threshold rate for movement to Be-filter position is nominally set to be 80,000 counts s^{-1} (adjustable by ground command), which corresponds to $\sim\text{M5}$ class flare as discussed later.

The filter wheel also has an additional position where a calibration source is mounted. The calibration source used is 100 mCi activity Fe-55 nuclide covered with a $3 \mu\text{m}$ thick titanium foil. This source generates four mono-energetic lines: Mn-K α and Mn-K β lines with energies of 5.9 keV and 6.49 keV, respectively, as well as Ti-K α and Ti-K β lines of energies 4.5 and 4.93 keV, respectively. Spectral response and gain of the instrument can be monitored by acquiring the spectrum of this calibration source. The filter wheel mechanism can be brought to the calibration position by ground command for in-flight calibration as and when required.

As the spacecraft attitude configuration is dictated by the requirement of observation of the Moon by other instruments and other mission operation constraints, the Sun's position varies with respect to the bore-sight of the XSM. Hence, in order to maximize the duration of observation of the Sun, the XSM is designed with a large field of view of 40° half cone angle. An aluminium collimator (or detector cap) with a thickness of 0.5 mm placed over the detector provides this wide field of view and, at the same time, restricts the aperture area such that the count rate remains within the instrument capability over a wide range of incident solar X-ray intensities. The collimator aperture of $\sim 0.7 \text{ mm}$, much smaller in comparison to the detector diameter of $\sim 6.18 \text{ mm}$, defines the instrument's geometric entrance area. As aluminium with thickness 0.5 mm is transparent to X-rays above $\sim 8 \text{ keV}$, the collimator is coated with $50 \mu\text{m}$ of silver on both sides to block X-rays up to 15 keV arriving from outside the XSM FOV. The coating on the bottom of the cap also ensures that the aluminium fluorescence lines from the cap do not reach the detector.

During the nominal operation phase, the attitude of the Chandrayaan-2 spacecraft is such that the yaw direction always points to the Moon (see figure 2 for the axis definition). All Moon-viewing instruments are mounted with their bore-sights in the yaw direction. Thus the spacecraft attitude is not fixed in the inertial reference frame. However, the orbital plane is fixed with respect to the inertial reference frame, and this results in different orientation of the orbital plane with respect to the Sun giving rise to the orbital seasons: 'dawn-dusk' (D-D) and 'noon-midnight' (N-M) [1], as shown in figure 3. The attitude of the spacecraft (other than yaw axis) is maintained according to these orbital seasons to optimize power generation. During the three months of D-D season surrounding the day when the orbital plane is perpendicular to the Moon-Sun vector, the spacecraft attitude is such that Sun is maintained in a yaw-roll plane. In this season, continuous observations of the Sun with XSM are possible. In the N-M season covering three months around the day when the Sun vector lies in the orbital plane of the spacecraft, the spacecraft attitude follows the orbital reference frame, and the Sun does not remain within the FOV of XSM for the entire orbit. Nominally, the XSM is expected to operate at all times when the Sun is within the FOV of the instrument.

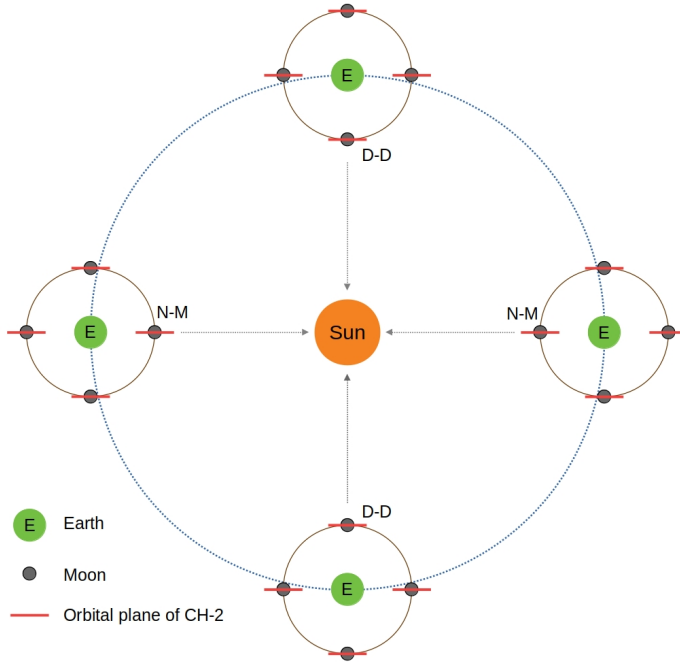


Fig. 3 Orbital seasons for Chandrayaan-2 spacecraft: ‘dawn-dusk’ (D-D) and ‘noon-midnight’ (N-M). On ‘dawn-dusk’ day, the orbital plane is perpendicular to the Moon-Sun vector, and on ‘noon-midnight’ day, it is parallel. The attitude of the spacecraft is defined differently during the three month seasons around both these days, as described in the text.

3 Calibration requirements for XSM

In case of an X-ray spectrometer like the XSM, the calibration primarily involves the accurate determination of the response matrix which dictates the relation between the incident photon spectrum, which is of interest, and the observed spectrum as:

$$C(I) = \int N(E) R(E, I) dE \quad (1)$$

where $R(E, I)$ is the response matrix of the instrument, $N(E)$ is the incident spectrum of the source in units of $photons\ s^{-1}cm^{-2}keV^{-1}$, and $C(I)$ is the observed spectrum having units $counts\ s^{-1}\ channel^{-1}$.

The XSM records the number of events detected (counts) every second in each ADC channel, also known as Pulse Height Analysis (PHA) channel. Gain parameters determine the mapping of the PHA channel to the nominal energy of the incident photon. As the gain usually varies with observing conditions, this mapping does not remain constant. In such a case, it is usual to resample the raw PHA spectrum into a pulse invariant (PI) channel space, correcting for the gain. This PI spectrum is used along with the response matrix to estimate

the incident spectrum based on the relation given in equation 1. We follow this approach for spectral analysis with the XSM.

Usually, the equation 1 is approximated as a finite sum with $R(E, I)$ defined over a grid of incident energies. This response matrix $R(E, I)$ can be divided into two components:

$$R(E, I) = ARF(E) RMF(E, I) \quad (2)$$

where $RMF(E, I)$ is the redistribution matrix that incorporates the spectral redistribution effects due to the detector characteristics and $ARF(E)$ is the ancillary response function (ARF) that includes the effective area of the instrument.

Thus, in order to infer the incident photon spectrum from XSM observations, gain parameters for the conversion of PHA spectrum to PI spectrum, the redistribution matrix, and the ancillary response function are to be determined during ground calibration. Considering these requirements, we investigate the linearity of the XSM over its entire energy range and then characterize the gain parameters over different operating conditions of temperature and incidence angle. The spectral redistribution function for the SDD used in the XSM is modeled using observed mono-energetic line spectra, and the effective area as a function of energy and angle is computed from experimental data and appropriate detector module parameters. We also study the stability of the spectral performance with flux, dead time, and pileup effects, which are of importance at high incident flux levels. In the subsequent sections, we describe these experiments carried out for the ground calibration of the XSM instrument and present the results.

4 Gain calibration

The relation between the peak channel recorded by a spectrometer for mono-energetic lines and the incident photon energies provides the gain parameters. If this relation is linear then only two parameters: gain and offset are sufficient to describe it. These parameters are typically estimated by acquiring the spectra of sources with mono-energetic lines at known energies and obtaining the respective peak channel positions by fitting the observed spectra.

The XSM instrument includes a calibration source, which emits four major lines at known energies, mounted on the filter wheel and is used for gain calibration. A spectrum of this calibration source obtained with the XSM at room temperature is shown in figure 4, where the major lines are identified. These lines were fitted with Gaussian models to obtain the peak channel position as well as the width. Peak channels and energies of these lines follow a linear relation. The spectral resolution, defined by the full width at half maximum (FWHM) of the line at 5.9 keV, is measured to be ~ 175 eV, which is better than the specified requirement of 180 eV.

However, these measurements are restricted to only a small range of 4.5 – 6.5 keV in the complete energy range of 1 – 15 keV of XSM. Hence, in order

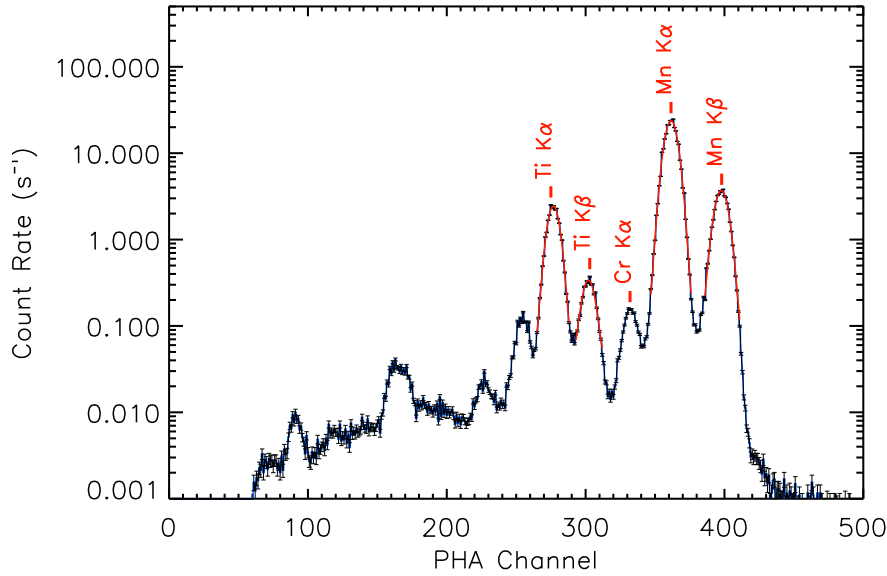


Fig. 4 A raw spectrum of the calibration source obtained using the XSM on the ground in PHA channels (up to ~ 8 keV) with the spectral lines identified. Four strongest lines were fitted with Gaussian to obtain the peak channels and width. The measured spectral resolution, defined by FWHM of the MnK α line at 5.9 keV, is 175 eV.

to verify the linearity over the entire energy range and to model the response function (as discussed in the next section), experiments were carried out with XSM at BL-03 [5] and BL-16 [6] X-ray beam lines of Indus-2 synchrotron facility at the Raja Ramana Center for Advanced Technology (RRCAT), Indore. Spectra were acquired with the XSM of the mono-energetic X-ray lines in the energy ranges of 1 – 2 keV (BL-03) and 4 – 15 keV (BL-16). All measurements were carried out at low incident rates ($\sim < 5000$ counts s^{-1}) and at approximately the same temperature so that the spectral response is not affected by these two factors. Observed X-ray lines were fitted with a Gaussian model to obtain the peak channel position at respective incident energy, as shown in figure 5, from which gain and offset are obtained with a straight line fit. A systematic error of 0.5 channel (8 eV) was added to the peak channel measurements to obtain a statistically acceptable fit. Figure 5 shows that the XSM has a linear gain relation over its entire energy range and that it provides energy measurements correct within 10 eV. Thus a linear fit with four lines from the in-built calibration source can provide the measurement of gain and offset of the instrument on the ground as well as during in-flight operations.

Gain parameters of X-ray spectrometers often show variation with temperature. Although the detector of XSM is maintained at a constant temperature, the instrument package temperature is expected to vary between -30° C and

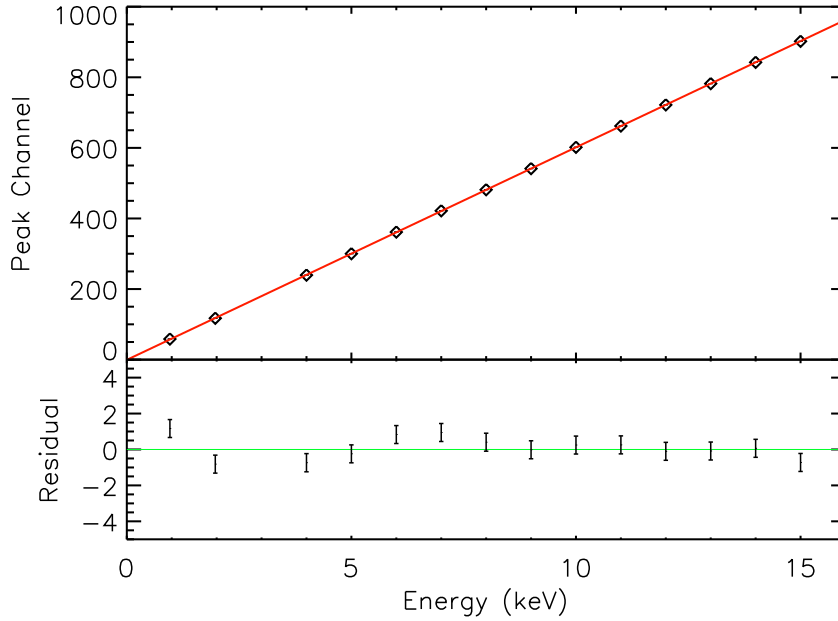


Fig. 5 Peak channel for mono-energetic lines plotted as a function of energy. Error bars are smaller than the symbol. The best fit line to the data is overplotted, and the residuals are shown in the bottom panel.

20° C during the in-orbit operations. As the components of the front-end electronics face this temperature variation, the gain may vary accordingly. Hence, the gain parameters have to be estimated as a function of the instrument temperature. For this purpose, the XSM spectra of radioactive sources were acquired over the entire operating temperature (with additional margin) during the thermovacuum test of the instrument, maintaining the detector at its nominal operating temperature of -35° C. In the initial part of the experiment, the calibration source that is part of the instrument was used, and for the latter part, an external source of Fe-55 was used.

Figure 6 shows the variation of the peak channel and FWHM of the 5.9 keV line for the entire duration. For comparison, the temperature profile and current drawn by the TEC of the detector that is proportional to the package temperature are also shown. Note that during the slow downward ramp of temperature, data were also acquired, keeping the instrument at a constant temperature but with the detector maintained at different temperatures in the range of -43° C to -23° C by changing the TEC set point. Measurements from the onboard source and the external source are marked with red and blue symbols, respectively, in the bottom panels of figure 6. It can be seen that there is a systematic variation in the peak channel (hence in the gain) with temperature. It can be noted that at the same temperature, peak channels for the 5.9 keV line from the onboard source and the external source are

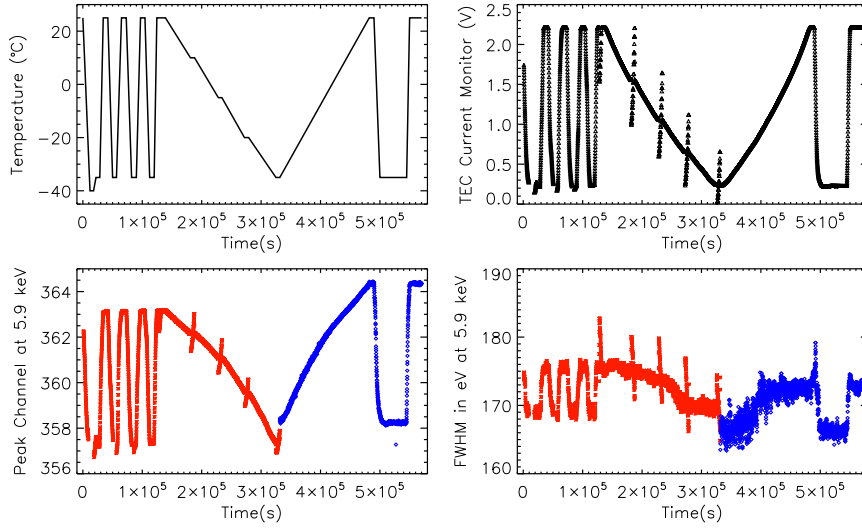


Fig. 6 Results of thermovacuum test of XSM are shown here. The upper two panels show the XSM package temperature profile during the test (left) and the TEC current monitor (right) corresponding to the same duration. The lower two panels show the peak channel (left) and FWHM (right) of the spectral line at 5.9 keV. Data obtained with the calibration source that is part of the instrument and an external source are shown with the red star and blue diamond symbols, respectively. During the slow downward ramp, the detector temperature was varied, keeping the package temperature constant at five values.

different; however, this is understood to be due to the dependence of gain on the interaction position of the photons in the detector and is discussed in detail in the subsequent paragraphs.

For both cases, the peak channel - energy relations at different temperatures were fitted with a straight line. As the offset did not show any significant variation, it was frozen to the value obtained from X-ray beam line measurements, and the gain was obtained as a function of TEC current monitor that acts as a proxy for the instrument package temperature. Figure 7 shows the gain plotted against the TEC current for the case of the onboard source (red) as well as the external source (blue). In both cases, gain shows a similar monotonic dependence on the TEC current. Measured values of gain at two other detector temperatures of -23°C and -42°C at few instances of ambient temperatures are also shown in the figure 7. In case of any requirement to operate the detector at temperatures different from the nominal plan, gain parameters can be derived from similar measurements available.

As indicated earlier, another factor affecting the gain in the XSM is the interaction position of X-rays in the detector. The SDD used in the XSM has a diameter of $\sim 6\text{ mm}$, whereas the aperture is of $\sim 0.7\text{ mm}$ diameter. When the source is on-axis to the instrument, the photons are incident at the center of the detector. As the angle of incidence increases, the interaction position on the detector moves away from the center and gets closer to its edge. With the

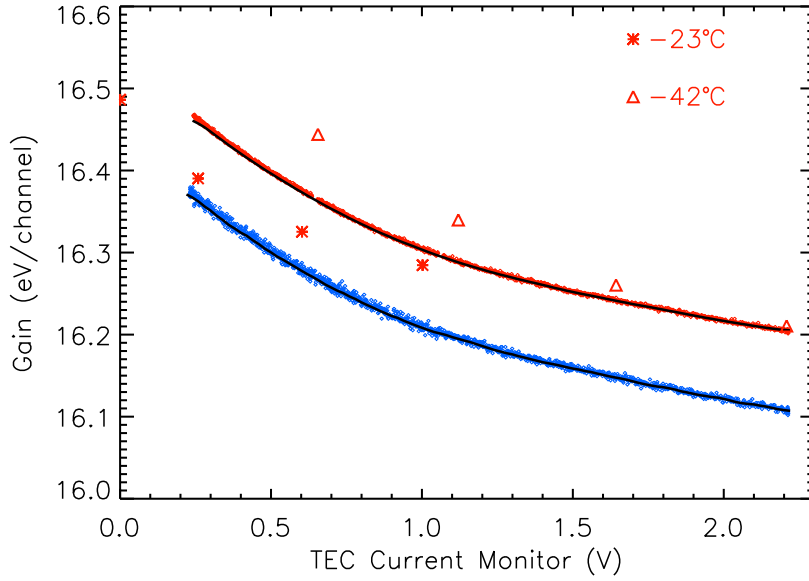


Fig. 7 The gain of the XSM obtained as a function of TEC current monitor for an external source shining at the center of the detector (blue) and the onboard calibration source that illuminates all regions of the detector (red) at the nominal detector temperature of -35°C . The black solid lines show the mean gain value over a grid of TEC current values. The measured gain at two other detector temperatures of -23°C and -42°C at a few instances of ambient temperature are also shown.

increase in distance of interaction position from the center where the anode is located, the charge collection efficiency and hence the gain is expected to vary. The onboard calibration source is a disk of $\sim 6\text{mm}$ diameter, and the placement is such that when it is in front of the detector, photons from the source will reach all positions of the detector. This explains the difference between the gain obtained using the calibration source and that obtained using the external source where the photons illuminate the center part of the detector alone.

In order to systematically investigate the dependence of the interaction position on the gain, an experiment was carried out where the detector without the collimator (detector cap) was illuminated at different positions with a pencil beam of diameter $\sim 0.7\text{mm}$ from a radioactive source of Fe-55. The experiment was carried out at a constant ambient temperature. The beam was systematically moved over a regular grid of positions on the detector with a step size of 0.5mm using motorized stages, and the spectrum was acquired in each case. Observed spectra were fitted with Gaussians for the lines at 5.9 and 6.5 keV to obtain their peak channel positions. Figure 8 shows the surface plots of the total count rate and peak channel for 5.9 keV line over the entire two-d grid of positions. It is seen that the peak channel shows a small

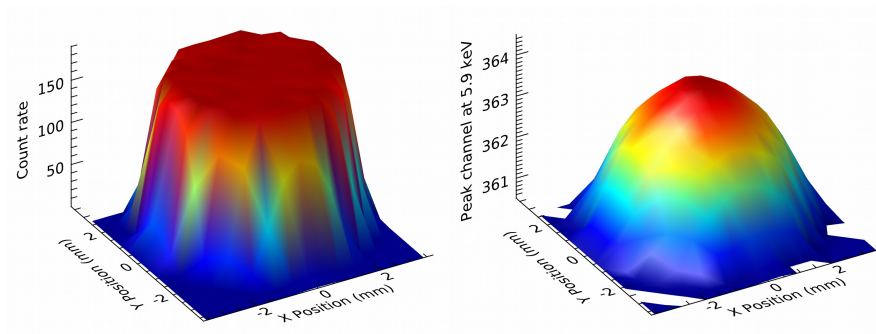


Fig. 8 Left: Surface plot showing the count rate over a grid of positions above the detector. Right: Peak channel for the 5.9 keV line as a function of interaction position on the detector, which shows a systematic trend. Colors are indicative of z-axis values.

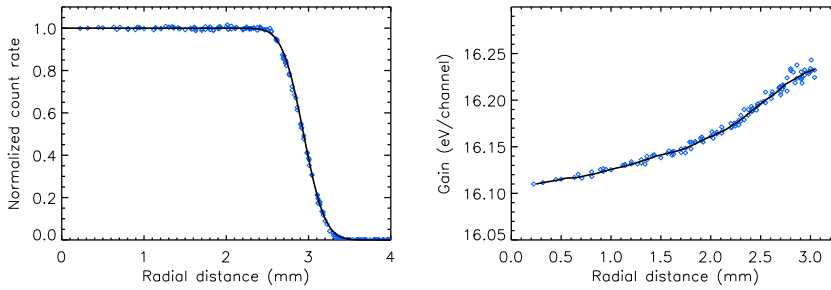


Fig. 9 Left: Normalized count rate at each grid point as a function of radial distance. The black solid line shows the expected trend when a Gaussian beam of 0.65 mm diameter moves from entirely within the active area of the detector of radius 3.09 mm to entirely outside its active area. Right: Gain for each grid point shown as a function of the radial distance from the center of the detector. The black solid line is the trend line obtained from the data points.

but definitive trend with the interaction position. Further, we compute the radial distance of each grid position from the center of the detector, and the count rate and gain at each position are plotted against the radial distance in figure 9. The observed trend of count rates is consistent with the expected trend (overplotted with line) when a Gaussian beam of 0.65 mm diameter scans over the active area of the detector having a radius of 3.09 mm , which confirms the manufacturer provided value of the detector active area.

The results from the experiments discussed above show that XSM has a linear relation between energy and PHA channel, and the gain shows a systematic variation with the TEC current and the interaction position on the detector, which is determined by the Sun angle. As both TEC current and Sun angle will be available at every second in the in-flight data, accurate gain correction can be applied to the raw solar spectrum to convert it into the PI

channels during ground processing. Further, any post-launch variation of the gain can be tracked using the onboard calibration source.

5 Spectral redistribution function

Photons of a given energy incident on an X-ray detector, are in general, recorded over a range of spectral channels of the instrument. This spectral redistribution occurs due to the inherent stochastic process of generation of the charge cloud, noise associated with the readout electronics, and other effects like incomplete charge collection. Spectral response of silicon detectors to mono-energetic X-rays typically consists of multiple components: a primary Gaussian photo-peak, an escape peak associated with Si fluorescence photons leaving the active detector volume, an exponential tail caused by incomplete charge collection, and a feature due to electron escape commonly referred to as shelf [7]. The spectral redistribution function forms a major component of the response matrix of the detector system and hence required to be determined accurately for inferring the incident photon spectrum from the observed spectrum.

In order to characterize the spectral response of the SDD, spectra of mono-energetic beams acquired with the XSM at RRCAT were utilized. Figure 10 shows the spectra observed with XSM for three incident photon energies. The spectra of mono-energetic lines show all the expected features, as seen from the figure.

We model the observed spectra for each energy with an empirical model that includes four components:

$$C(E_i, E_0) = P1 + P2 + T + S \quad (3)$$

where, $C(E_i, E_0)$ is the count spectrum in channel I (with nominal energy E_i) for an incident photon energy of E_0 . The terms on the right hand side correspond to photo-peak ($P1$), escape peak ($P2$), exponential tail (T), and shelf (S). The primary and escape peaks are modelled with Gaussians defined as:

$$P1(E_i, E_0) = \frac{1}{\sqrt{2\pi}\sigma} \exp\left[-\frac{(E_i - E_0)^2}{2\sigma^2}\right] \quad (4)$$

$$P2(E_i, E_0) = I_{esc} \frac{1}{\sqrt{2\pi}\sigma} \exp\left[-\frac{(E_i - (E_0 - 1.74))^2}{2\sigma^2}\right] \quad (5)$$

where, σ is the standard deviation of the Gaussian and I_{esc} is the relative strength of escape peak with respect to the primary peak. The tail component is modelled with an exponential function multiplied with complementary error function (erfc) as:

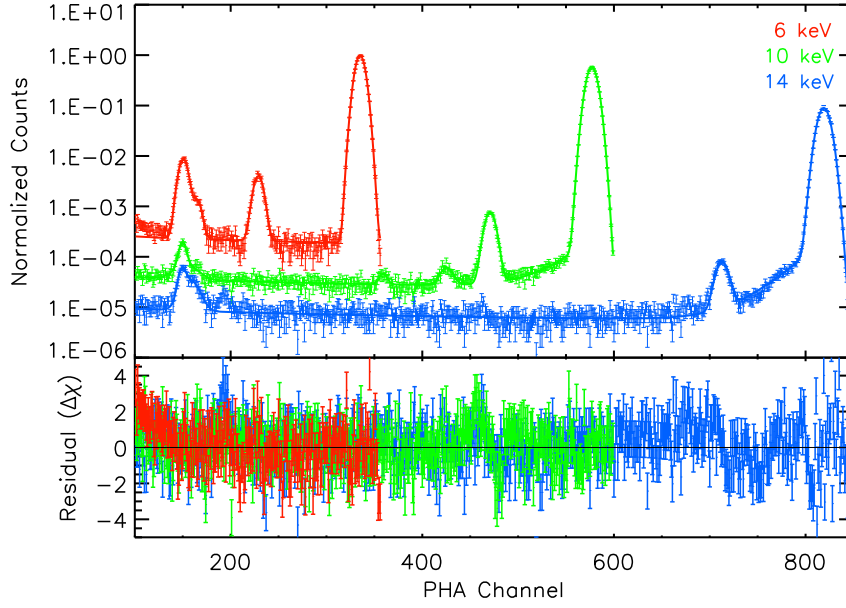


Fig. 10 XSM spectra of mono-energetic X-ray beams at three energies. Note that for better clarity the spectra are shown with vertical offsets. Best fit spectral response models are overlotted with solid lines, and the bottom panel shows the residuals in terms of sigmas with error bars of size one.

$$T(E_i, E_0) = I_{tail} \exp\left[\frac{(E_i - E_0)}{\beta}\right] * \operatorname{erfc}\left[\frac{(E_i - E_0)}{(\sqrt{2}\sigma)} + \frac{\sqrt{2}\sigma}{2.0\beta}\right] \quad (6)$$

where, I_{tail} is the relative strength of the tail component and β is the parameter defining the slope of the tail. The shelf component in the model is given by:

$$S(E_i, E_0) = I_{shelf} \left(\frac{E_i}{10}\right)^{-\alpha} \left(\operatorname{erf}\left[\frac{E_i - 1.74}{\sqrt{2}\sigma}\right] + 2.0\right), \text{ when } E_i < E_0 \quad (7)$$

Here, the relative strength of the component is determined by I_{shelf} and the parameter α is the power-law index.

This empirical model for the SDD spectral response was implemented as a local model in pyXspec, the python interface of the spectral fitting tool XSPEC [8]. The model parameters include the relative strengths of all components, the width of the Gaussian (σ), tail slope β , and shelf power-law index α . The observed spectra for all energies were fitted with the model. Additional line components were added in the model in cases where peaks, such as that of argon arising from the air in between, are present in the spectrum, to obtain

proper fit (see figure 10). During the fitting, it was noted that the parameters α , β , and I_{shelf} are independent of energy, and they were frozen to constant values to obtain the final best fit values for rest of the parameters. Best fit models are overplotted on the observed spectra shown in figure 10. Residuals plotted in the bottom panel of the figure show that the model describes the observed spectra well.

In order to derive the spectral response of the instrument over the full energy range of 1 – 15 keV, the model parameters are required as a function of energy. Figure 11 shows the three free parameters of the model plotted as a function of incident photon energy. The full width at half maximum (FWHM) of the Gaussian, defined as 2.35σ , to a first-order has a dependence on the square root of energy. However, the best fit is obtained with the inclusion of a second-order term using a function of the form:

$$\text{FWHM} (E) = 2.35 \sqrt{a + bE + cE^2} \quad (8)$$

In this equation, FWHM has units of eV and E is in keV. The best fit curve is overplotted with the data points in the figure 11.

The second panel of the figure 11 shows the relative intensity of the escape peak as obtained from the spectral fits. As escape peaks are present only when incident photon energy is higher than the K-edge energy of Si, this parameter is not applicable for the monochromatic line at 1 keV. For the line at 2 keV, the escape peak energy is well below the lower energy threshold of XSM. Hence the measurement of escape peak strength is available only for 6 keV and above. As the measurements are not available near to the K-edge energy, we resort to simulations with Geant4 toolkit [9] to obtain escape peak strength over the entire energy range. A silicon detector is modeled in Geant4 with the dimensions matching the detector used in XSM. The detector is illuminated with a large number of photons of each photon energy, and energy deposited is recorded. From the simulation output, the intensity of the escape peak is computed, and the result is overplotted as a solid line in figure 11, which is found to match with the measured values at few energies. The third free parameter, the intensity of the tail component, shows an increasing trend with energy. It is fitted with a power-law model:

$$I_{tail}(E) = I_{tail}^0 \left(\frac{E}{15} \right)^\gamma \quad (9)$$

The best fit model overplotted on the data is shown in the bottom panel of the figure 11.

Thus, we obtain all the parameters of the spectral redistribution function model, as tabulated in table 2. For FWHM and intensity of the tail component, parameters defining the energy dependence in equations 8 and 9 are given in the table. With these parameters, we evaluate the spectral redistribution function at a discrete set of energies to generate the redistribution matrix of XSM, which is required in spectral analysis. It is also noted that specific PHA channels (typically channel numbers 2^n with $n \geq 4$) have systematically

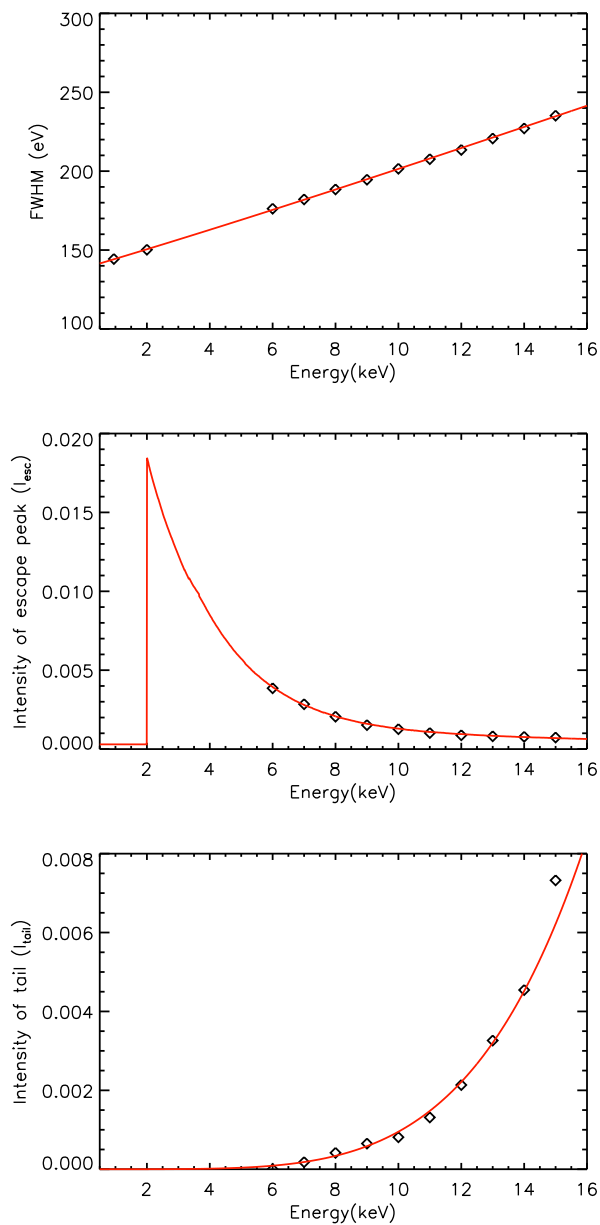


Fig. 11 Spectral response model parameters obtained from fitting mono-energetic spectra: FWHM (top), the relative intensity of the escape peak (middle), and intensity of the tail component (bottom) are plotted as a function of energy. Statistical errors are smaller than the symbol size. The red solid lines show the best fit models given by equations 8 and 9, in the case of FWHM and intensity of the tail component, respectively, whereas for the escape peak intensity (middle panel), the line represents the result from Geant4 simulation.

Table 2 Parameters of spectral redistribution function model of XSM defined by equations 3-9.

Parameter	Value
a	3528.9
b	299.04
c	9.41
I_{esc}	Geant4 Simulation
I_{tail}^0	6.21×10^{-3}
γ	4.63
β	0.5
I_{shelf}	10^{-4}
α	0.3

higher or lower counts than expected from the redistribution model, and this is attributed to the ADC characteristics. Systematic errors for each PHA channel were estimated from the ground calibration data, and typical errors are $\lesssim 2\%$ with a maximum up to 10% for a few channels. These channel-wise systematic errors are incorporated into the errors on the spectral measurements. As all components of the mono-energetic response of the detector and electronics are incorporated in the model, it provides an accurate redistribution matrix.

6 Ancillary response function

The ancillary response function (ARF) or the effective area of XSM includes geometric area, collimator response, and detection efficiency and transmission of entrance windows as a function of energy. As the angle subtended by the Sun with respect to the axis of XSM is expected to vary, the effective area needs to be estimated as a function of incidence angle.

The primary component of the effective area is the geometric area, which in the case of the XSM, is defined by the aperture on the aluminium collimator (detector cap). The collimator is designed to have an aperture of 0.7 mm; however, it is essential to measure the fabricated unit's aperture as it may deviate from the design value. As the aperture size may vary between the multiple fabricated units, measurements of diameter across various directions were carried out for all of them with an optical projection facility. The unit with the least non-uniformity in aperture was used for the flight model of the instrument (photograph shown in figure 12 left panel). For this unit, the diameter of the aperture was measured to be 0.684 mm, which defines the on-axis geometric area of the instrument.

The efficacy of the aluminium collimator, which is coated with 50 μm silver on both sides, to block the X-rays from all directions other than the aperture was also verified experimentally. A specially made silver-coated collimator without any aperture was assembled in front of the detector, illuminated with X-rays from a miniature X-ray generator (Amptek Mini-X with a gold target) and the spectrum was recorded. Spectrum without the collimator directly exposing the detector was also recorded, and from the ratio of both

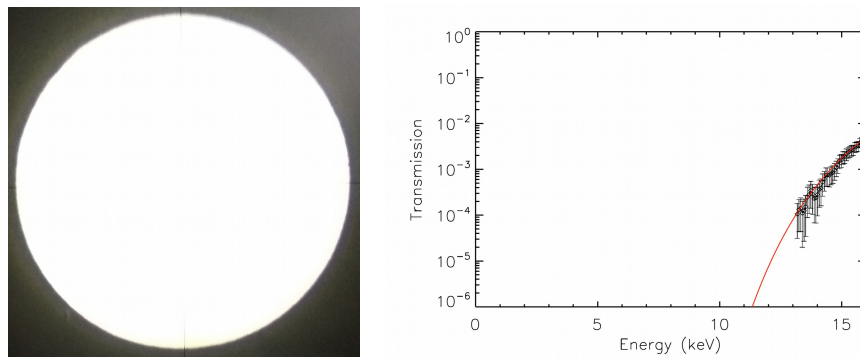


Fig. 12 Left: Photograph showing the aperture of the XSM collimator. Right: Transmission of the silver-coated ($50 \mu\text{m}$ on both sides) collimator obtained as the ratio of X-ray gun spectrum recorded with specially made collimator without any aperture to that recorded without the collimator. The red solid line shows the expected transmission of the collimator.

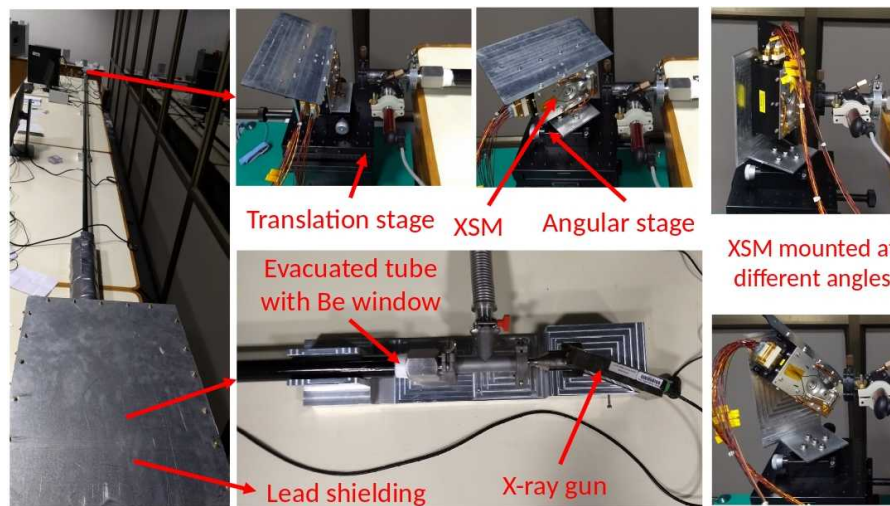


Fig. 13 Experimental setup for characterization of the angular response of the XSM. X-rays from a miniature X-ray source was collimated over a distance of six meters using an evacuated tube or beam line. At the other end of the beam line, the XSM sensor package was mounted on rotation and translation stages. XSM data acquired at different angles of the instrument with the incident beam were used to obtain the relative area as a function of angle. Measurements were also carried out with the sensor package mounted in different orientations, as shown in the right-most images to determine the response across different azimuthal directions.

these spectra, the transmission of the collimator was obtained as a function of energy, which is shown in the right panel of figure 12. This demonstrates that the collimator efficiently blocks X-rays over the energy range of XSM as required.

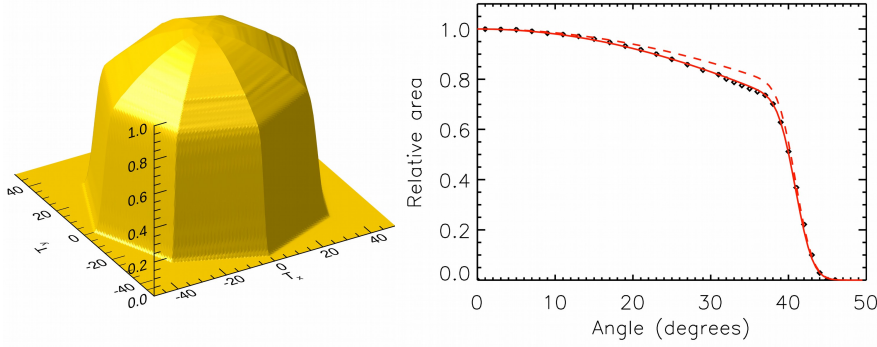


Fig. 14 Left: Surface plot showing relative area measured as a function of polar angle at eight azimuthal angles. Right: Area as a function of polar angle at an azimuth angle of zero degrees. The red dashed line shows the trend expected with the projection effect, and the red solid line is an empirical model that explains the observed behavior.

To determine the next component of ARF, the collimator response as a function of incidence angle, an experiment was carried out with a six-meter long temporary beam line, as shown in figure 13. The beam line consisted of an evacuated steel tube with Beryllium windows on both ends to allow entry and exit of X-rays. A miniature X-ray source was placed on one end, and the XSM sensor package was mounted on translational and angular stages at the other end of the beam line. The design of the mounting setup ensured that the rotation of the sensor package was with respect to the center of the aperture. Before the measurement of angular response, the X-ray beam was aligned to the XSM aperture by adjusting the position of the sensor package with the translation stage. Data were acquired with the XSM at different angles of the instrument Z-axis (detector normal) with respect to the beam direction. A similar exercise was carried out by mounting the XSM in three more orientations to obtain the response across different azimuthal angles.

Count rates at each angular position were determined from the observed spectra, and the relative area as a function of polar and azimuthal angles (with respect to the instrument reference frame defined in figure 2) was estimated. Figure 14 left panel shows the three-dimensional surface plot of the angular response of XSM across eight azimuthal angles. These measurements show that the field of view of XSM is symmetric, and the null points of the FOV are approximately at 44 degrees. The right panel of the figure shows the angular response with polar angle along the azimuthal angle of zero degrees. The red dashed line overlotted on the figure shows the expected variation in angular response, considering only the projection factor along with the edge effects, and the data points are clearly lower than the prediction. Further, we model the observed angular response with a function having a $\cos^\alpha(\theta)$ dependence instead of $\cos(\theta)$ dependence, and the model is shown with a solid red line in the figure. It is seen that the observed angular response is explained with an index of $\alpha \approx 1.4$. The departure from the expected cosine behavior is

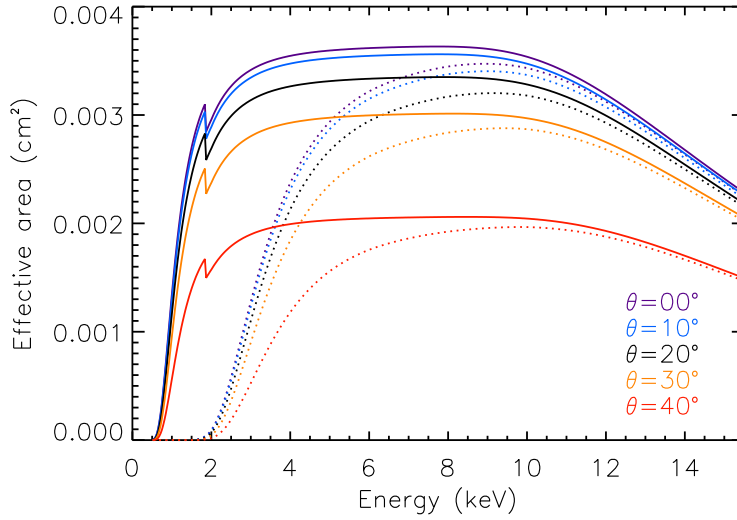


Fig. 15 The effective area of the XSM as a function of energy at different angles of incidence. Solid lines correspond to the effective area without the Be filter, whereas the dotted lines show the effective area with the Be filter in front of the detector.

attributed to the fact that the aperture is not a two-dimensional circle, but a three-dimensional cylinder of finite thickness of the order of $50 \mu\text{m}$.

Other factors that contribute to the effective area are the thicknesses of the detector chip, dead layers, the Be entrance window, and the Be filter on the filter wheel mechanism. An attempt was made to measure the parameters that are internal to the detector module with beamline experiments; however, there were very large uncertainties due to various other factors. Hence, we decided to use the manufacturer provided values for the thicknesses of the detector chip ($450 \mu\text{m}$), deadlayers ($0.1 \mu\text{m}$ Si and 80nm SiO_2), and Be entrance window ($8 \mu\text{m}$). For the additional Be filter, physical measurement of the thickness, as well as the measurement of the transmission of X-rays, were carried out to obtain the final value of $254 \mu\text{m}$, which is within limits specified by the manufacturer. The overall detector efficiency as a function of energy is then estimated for different off-axis angles considering the transmission by the deadlayers, entrance window, and filter and the absorption by the silicon chip using the attenuation coefficients of the materials from the NIST database.

Taking into account the geometric area, collimator response, and detector efficiency, the estimated effective area of the XSM at different incidence angles are shown in figure 15. Solid lines correspond to the effective area without the additional thick Be filter, whereas the dotted lines correspond to the cases with the filter.

7 Spectral performance with incident rate

Since the incident count rate of the solar X-rays is expected to vary over a wide range, one important aspect to examine for a solar X-ray spectrometer is the stability of spectral performance with count rate. X-ray spectrometers with analog front-end electronics typically exhibit a change in the peak channel position and degradation of spectral resolution with an increase in count rate.

In order to characterize the performance of the XSM with incident count rate, two sets of experiments were carried out: one with mono-energetic lines from X-ray beams at RRCAT and another with a miniature X-ray generator. XSM spectra were acquired for beam energies of 5 keV and 12 keV for a range of incident count rates. The count rates were varied with the help of slits available in the beam line.

With the miniature X-ray generator, XSM spectra were acquired for different count rates by placing the source at different distances from the instrument. Distances were chosen such that the count rates span from few thousand counts s^{-1} to $\sim 4 \times 10^5 \text{ counts s}^{-1}$. X-ray spectrum from the gun includes a Bremsstrahlung continuum and L lines of the target material gold. The spectral performance is evaluated with the $L - \alpha$ line of gold at 9.7 keV.

For all three cases, spectral lines were fitted with Gaussian to obtain the peak channel position and the FWHM. Figure 16 shows these parameters for three energies plotted against the event rate. It can be seen from the figure that for all three energies, the peak channel and FWHM show variation above threshold count rates demarcated by vertical dotted lines. As one would expect, the threshold rate is the highest for 5 keV, the lowest of three energies, and decreases at higher energies. As most of the events in the solar spectrum would be at lower energies, it is expected that spectral performance during solar observations would be closer to the 5 keV case where there is no significant degradation up to $10^5 \text{ counts s}^{-1}$. However, to be on a safer side, we consider that the spectral performance is stable up to $8 \times 10^4 \text{ counts s}^{-1}$ and have finalized this as the threshold rate for automated movement of the filter wheel to the Beryllium filter position.

Simulations using the XSM response matrix and the CHIANTI atomic database [10, 11] to estimate the expected count rate for different levels of solar activity, details of which will be reported elsewhere, show that for M5 class of solar flares, the XSM will detect $\sim 8 \times 10^4 \text{ counts s}^{-1}$. Hence, the transition from open to the Be filter position is expected at this level of activity. With the Be filter, the limiting rate of $8 \times 10^4 \text{ counts s}^{-1}$ will be reached during X5 class of flares, beyond which the spectral performance will begin to degrade.

We also examined the stability of spectral performance with the incident rate at different detector temperatures. This was done by acquiring spectra from the miniature X-ray source with different count rates and setting the detector temperature at specific values. Figure 17 shows the variation of FWHM with count rate at different detector temperatures. The constant value of FWHM at lower count rates shows a systematic increase with the temperature; however, the threshold event rate where the FWHM degrades signifi-

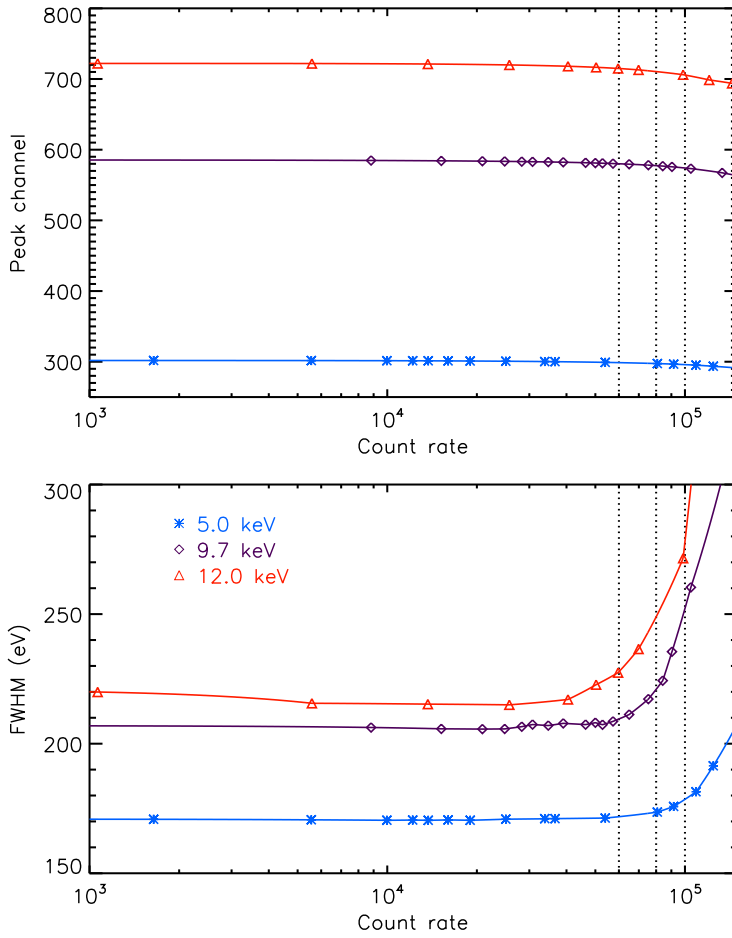


Fig. 16 Peak channel (top) and FWHM (bottom) of spectral lines at three energies measured with the XSM as a function of incident rate. Vertical dotted lines show the approximate count rate above which the spectral performance degrades significantly for all cases. For the 9.7 keV line, spectral performance is stable up to an incident rate of 80,000 $counts\ s^{-1}$.

cantly does not seem to depend on the temperature. Hence, even if there is a requirement to operate the XSM at higher detector temperatures, it will not affect the dynamic range of the instrument.

8 Dead time and pileup

All photon counting systems have a short but finite dead time. Once an X-ray photon interacts, it cannot sense another photon interaction while the detector and the front-end electronics process the signal from the first photon.

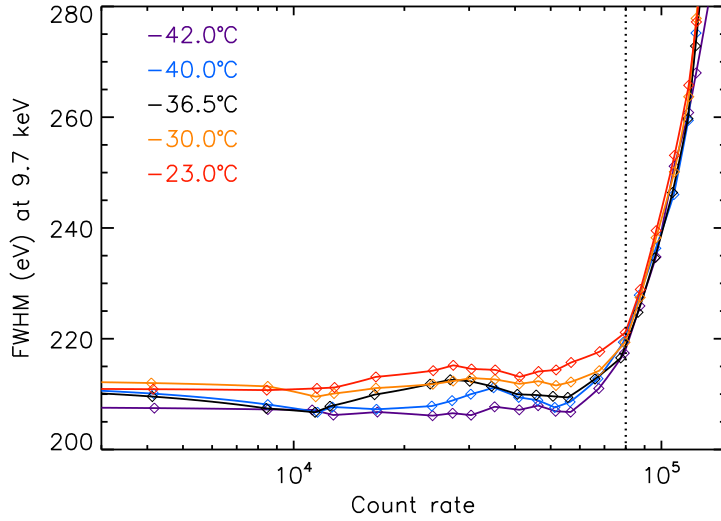


Fig. 17 FWHM at 9.7 keV as a function of count rate with the detector maintained at different temperatures. The FWHM increases with the detector temperature; however, it can be seen that the count rate at which the performance starts to degrade is not significantly dependant on the detector temperature.

The effects of dead time, which is typically of the order of few microseconds, are important when the incident photon rate is high, as expected during high-intensity flares for XSM. To obtain accurate flux from the observed spectrum, the exposure times are to be corrected for the dead time effects.

The XSM front-end electronics require $\sim 3 - 5 \mu s$ to properly digitize the height of the electronic pulse generated by any photon interaction. The first microsecond is an absolute dead time, during which two independent photon interactions cannot be distinguished separately. If the second photon interacts after one microsecond but within the digitization dead time, it can be identified as an independent interaction (counted as event triggers), but its energy measurement is not possible. The exact dead time of the analog front-end electronics depends on the energy of the incident photon and hence is difficult to correct. Therefore, XSM implements a fixed dead time of $5 \mu s$ (default value, can be changed by a command to $10 \mu s$ if needed) in the FPGA based digital readout system. Further, the XSM implements this fixed digital dead time in a *paralyzable* mode [12], i.e., event triggers that occur within the dead time are not considered for energy measurements, but they extend the dead time further. The event triggers themselves do not represent the actual incident rate as they are also affected by the absolute dead time of $\sim 1 \mu s$. However, in this case, the dead time behavior is expected to be similar to the *non-paralyzable* model.

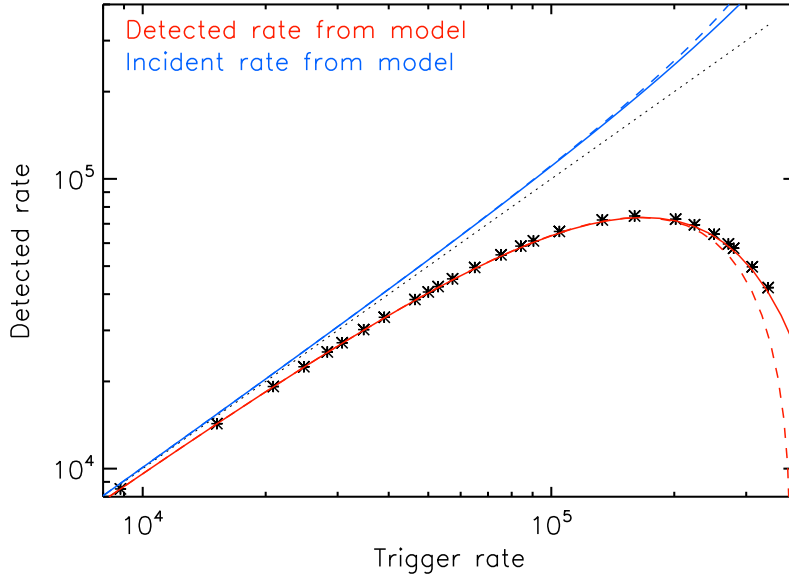


Fig. 18 The detected event rate is shown as a function of event trigger rate (black star symbols). Red lines show the expected trends of detected event rate with the trigger rate, and blue lines show the incident rates. Solid and dashed lines correspond to the predictions with *non-paralyzable* and *paralyzable* dead time models for event triggers.

In order to verify the dead time behavior of the instrument, the data acquired at different incident rates with the miniature X-ray gun, as described in section 7, was used. From the data, trigger rate and the rate of recorded events for each case were computed and are plotted as data points in figure 18.

In order to compare with the observations, trigger and detected rates for a range of actual incident rates are computed considering the non-paralyzable and paralyzable models for trigger and detected events, respectively, using the following equations [12]:

$$n_t = \frac{n_a}{1 + n_a \tau_1} \quad (10)$$

$$n_d = n_a \exp(-n_a \tau_2) \quad (11)$$

where n_t , n_d , and n_a are the trigger, detected, and actual rates, respectively. Dead times involved are τ_1 and τ_2 . Model predictions for $\tau_1 = 0.96 \mu s$ and $\tau_2 = 5 \mu s$ are plotted with red solid line in the figure 18, which matches the observations. For comparison, the expected behavior for event triggers in the case of paralyzable model is shown with dashed lines that deviate from the observations. Blue lines in the figure show the incident rates as a function of trigger rates for both cases.

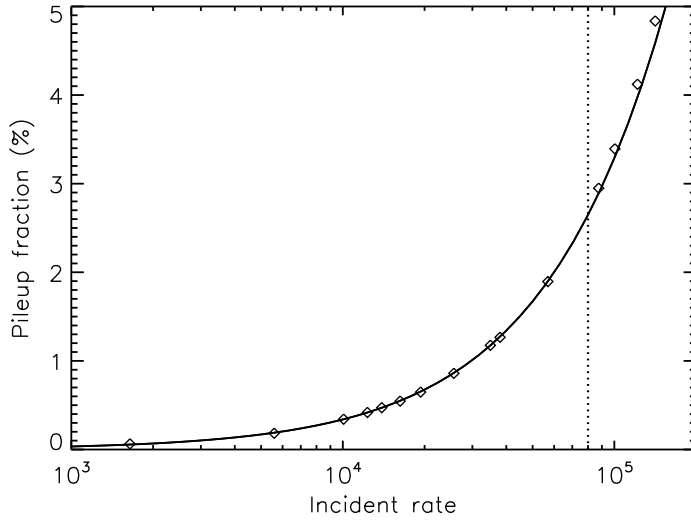


Fig. 19 Percentage of incident events that are affected by pulse pileup in XSM spectrum as a function of the incident rate as measured from the experiment are shown as the data points. The black solid line is the prediction based on the pulse-peaking time ($0.35 \mu\text{s}$) of XSM. The vertical dotted line corresponds to the incident rate of $80,000 \text{ counts s}^{-1}$, the threshold rate for no variation in spectral performance.

With the experimental verification of the dead time characteristics of the XSM, the model and the obtained dead time values can be used to correct the dead time effects in the observed flux. This is done by modifying the exposure time of the observed spectrum by:

$$T_{live} = T_{exp} * \frac{n_d}{n_t} * (1 - n_t \tau_1) \quad (12)$$

where the symbols have the same meaning as earlier. It can be noted that, for low count rates, the correction term is negligible, whereas, at higher rates, this becomes important. XSM data analysis software includes this correction for the exposure time.

Another effect that is important at high count rates for X-ray detectors is the pulse pileup. When the incident rates increase, there is a chance that two photons are incident on the detector within the charge-readout time scales, which is less than a microsecond in the case of XSM. In that case, the detector would record only one event with the measured energy equivalent to the sum of energies of both photons, skewing the measured spectrum to higher energies than the actual.

In order to investigate the pileup effects in XSM, spectra of the mono-energetic line at 5 keV, obtained from the RRCAT facility, with different incident rates were used. As the incident rate increases, the obtained spectrum has events with energies above 5 keV that are due to the pileup of photons.

The fraction of the total events that are affected by pileup was computed by taking the ratio of events in the spectrum above 5 keV with the total. This fraction is then corrected for the dead time effects, as discussed earlier. Figure 19 shows the measured fraction of incident photons that suffered pileup in the XSM detector as a function of incident rate. The same obtained from a model with the XSM pulse peaking time of $0.35 \mu s$ is overplotted with a solid line and was found to be consistent with the measurements. It may be noted that the pileup fraction is independent of incident photon energy; hence, these measurements are directly applicable to solar observations. As discussed in the previous section, the XSM is expected to operate up to an incident rate of $80,000 \text{ counts s}^{-1}$ until which there is no spectral degradation, and it is seen from the figure 19 that the pileup fraction is less than 3% in this range. Hence, the effect of pileup can be safely ignored for the spectral analysis.

9 Summary

The results of ground calibration of the Chandrayaan-2 *Solar X-ray Monitor* are presented. Dedicated experiments were carried out to determine various parameters of the instrument response. The linearity of the spectrometer was established over the entire energy range, and the dependency of the gain parameters on temperature and interaction position was parameterized from extensive experimental data such that the uncertainty in energy measurement is less than 10 eV. The stability of spectral performance with incident flux was assessed and it has been established that it remains unaffected up to a count rate of $80,000 \text{ counts s}^{-1}$ suggesting that spectroscopy with the XSM in the 1–15 keV energy range is feasible for flares up to $\sim M5$ class, and up to $\sim X5$ class with the low energy threshold increased to 2 keV using the beryllium filter. For this operating count rate range, the dead time correction method has been established, and pileup effects were shown to be unimportant. With a suite of observations of mono-energetic X-ray lines, the spectral redistribution function of the detector was modeled with empirical functions having energy dependant parameters, taking into account all features to provide an accurate redistribution matrix. The on-ground estimate of the effective area as a function of energy and angle was obtained from the experimental measurements of the geometric area and collimator response, and the manufacturer provided values of the detector module parameters.

Thus, all aspects of the XSM response, required to infer the incident photon spectrum from the observed count spectrum, have been well-calibrated. The Chandrayaan-2 mission was launched on 22 July 2019, and the XSM began its operations in early September 2019. Preliminary observations suggest that the instrument is performing as expected ¹. Details of in-flight performance and refinement of the calibration will be reported elsewhere.

¹ See the update dated October 10, 2019 at <https://www.isro.gov.in/chandrayaan2-latest-updates>

Acknowledgements The XSM payload was designed and developed by Physical Research Laboratory (PRL), Ahmedabad, supported by the Department of Space, Govt. of India. PRL was also responsible for the development of the required data processing software, overall payload operations, and data analysis of XSM. The filter wheel mechanism for the XSM was provided by U. R. Rao Satellite Centre (URSC), Bengaluru, along with Laboratory for Electro-Optics Systems (LEOS), Bengaluru. Thermal design and analysis of the XSM packages were carried out by URSC whereas Space Application Centre (SAC) supported in mechanical design and analysis. SAC also supported in the fabrication of the flight model of the payload and its test and evaluation for the flight use. We thank various facilities and the technical teams of all the above centres for their support during the design, fabrication, and testing of this payload. X-ray beam lines BL-03 and BL-16 of the Indus-2 synchrotron facility at the Raja Ramanna Center for Advanced Technology, Indore were used in the calibration of the XSM. The Chandrayaan-2 project is funded and managed by the Indian Space Research Organisation (ISRO).

References

1. M. Vanitha, P. Veeramuthuvel, K. Kalpana, G. Nagesh, in *Lunar and Planetary Science Conference* (2020), Lunar and Planetary Science Conference, p. 1994
2. V. Radhakrishna, A. Tyagi, S. Narendranath, K. Vadodariya, R. Yadav, B. Singh, G. Balaji, N. Satya, A. Shetty, H.N. Suresh Kumar, Kumar, S. Vaishali, N.S. Pillai, S. Tadeipalli, V. Raghavendra, P. Sree Kumar, A. Agarwal, N. Valarmathi, *Current Science* **118**(2), 219 (2020). DOI 10.18520/cs/v118/i2/219-225
3. M. Shanmugam, S.V. Vadawale, A.R. Patel, H.K. Adalaja, N.P.S. Mithun, T. Ladiya, S.K. Goyal, N.K. Tiwari, N. Singh, S. Kumar, D.K. Painkra, Y.B. Acharya, A. Bhardwaj, A.K. Hait, A. Patinge, A.h. Kapoor, H.N.S. Kumar, N. Satya, G. Saxena, K. Arvind, *Current Science* **118**(1), 45 (2020). DOI 10.18520/cs/v118/i1/45-52
4. B. Joshi, R. Bhattacharyya, K.K. Pandey, U. Kushwaha, Y.J. Moon, *A&A* **582**, A4 (2015). DOI 10.1051/0004-6361/201526369
5. M. Modi, R. Gupta, S. Kane, V. Prasad, C. Garg, P. Yadav, V. Raghuvanshi, A. Singh, M. Sinha, in *AIP Conference Proceedings*, vol. 2054 (2019), vol. 2054, p. 060022. DOI 10.1063/1.5084653
6. M. Tiwari, P. Gupta, A. Sinha, S. Kane, A. Singh, S. Garg, C. Garg, G. Lodha, S. Deb, *Journal of synchrotron radiation* **20**, 386 (2013). DOI 10.1107/S0909049513001337
7. F. Scholze, M. Procop, *X-ray Spectrometry* **38**(4), 312 (2009). DOI 10.1002/xrs.1165
8. K.A. Arnaud, in *Astronomical Data Analysis Software and Systems V, Astronomical Society of the Pacific Conference Series*, vol. 101, ed. by G.H. Jacoby, J. Barnes (1996), *Astronomical Society of the Pacific Conference Series*, vol. 101, p. 17
9. S. Agostinelli, J. Allison, K. Amako, J. Apostolakis, H. Araujo, P. Arce, M. Asai, D. Axen, S. Banerjee, G. Barrand, F. Behner, L. Bellagamba, J. Boudreau, L. Broglia, A. Brunengo, H. Burkhardt, S. Chauvie, J. Chuma, R. Chytrcek, G. Cooperman, G. Cosmo, P. Degtyarenko, A. Dell'Acqua, G. Depaola, D. Dietrich, R. Enami, A. Feliciello, C. Ferguson, H. Fesefeldt, G. Folger, F. Foppiano, A. Forti, S. Garelli, S. Giani, R. Giannitrapani, D. Gibin, J.G. Cadenas, I. Gonzlez, G.G. Abril, G. Greeniaus, W. Greiner, V. Grichine, A. Grossheim, S. Guatelli, P. Gumplinger, R. Hamatsu, K. Hashimoto, H. Hasui, A. Heikkinen, A. Howard, V. Ivanchenko, A. Johnson, F. Jones, J. Kallenbach, N. Kanaya, M. Kawabata, Y. Kawabata, M. Kawaguti, S. Kelner, P. Kent, A. Kimura, T. Kodama, R. Kokoulin, M. Kossov, H. Kurashige, E. Lamanna, T. Lampn, V. Lara, V. Lefebure, F. Lei, M. Liendl, W. Lockman, F. Longo, S. Magni, M. Maire, E. Medernach, K. Minamimoto, P.M. de Freitas, Y. Morita, K. Murakami, M. Nagamatu, R. Nartallo, P. Nieminen, T. Nishimura, K. Ohtsubo, M. Okamura, S. O'Neale, Y. Oohata, K. Paech, J. Perl, A. Pfeiffer, M. Pia, F. Ranjard, A. Rybin, S. Sadilov, E.D. Salvo, G. Santin, T. Sasaki, N. Savvas, Y. Sawada, S. Scherer, S. Sei, V. Sirotenko, D. Smith, N. Starkov, H. Stoecker, J. Sulkimo, M. Takahata, S. Tanaka, E. Tcherniaev, E.S. Tehrani, M. Tropeano, P. Truscott, H. Uno, L. Urban, P. Urban, M. Verderi, A. Walkden, W. Wander, H. Weber, J. Wellisch, T. Wenaus, D. Williams, D. Wright,

- T. Yamada, H. Yoshida, D. Zschiesche, Nuclear Instruments and Methods in Physics Research Section A: Accelerators, Spectrometers, Detectors and Associated Equipment **506**(3), 250 (2003). DOI [https://doi.org/10.1016/S0168-9002\(03\)01368-8](https://doi.org/10.1016/S0168-9002(03)01368-8). URL <http://www.sciencedirect.com/science/article/pii/S0168900203013688>
10. K.P. Dere, E. Landi, H.E. Mason, B.C. Monsignori Fossi, P.R. Young, *A&AS***125**, 149 (1997). DOI 10.1051/aas:1997368
 11. G. Del Zanna, K.P. Dere, P.R. Young, E. Landi, H.E. Mason, *A&A***582**, A56 (2015). DOI 10.1051/0004-6361/201526827
 12. G.F. Knoll, *Radiation detection and measurement* (2000)